Nanocrystal growth, magnetic and electrochemical properties of NiZn ferrite

R.M. Freire [a], P.G.C. Freitas [b], W.S. Galvao [b], L.S. Costa [c], T.S. Ribeiro [d], I.F. Vasconcelos [d], J.C. Denardin [a], R.C. de Oliveira [e], C.P. Sousa [e], P. de-Lima-Neto [e], A.N. Correia [e], P.B.A. Fechine [b], *

[a] *Departamento de Física, Universidad de Santiago de Chile, USACH, Av. Ecuador, 3493, Santiago, Chile*
[b] *Grupo de Química de Materiais Avançados (GQMat), Departamento de Química Analítica e Físico-Química, Universidade Federal Do Ceará – UFC, Campus Do Pici, CP 12100, CEP 60451-970, Fortaleza, CE, Brazil*
[c] *Laboratório Nacional de Nanotecnologia (LNNano), Centro Nacional de Pesquisa Em Energia e Materiais (CNPEM), CEP 13083-970, Campinas, São Paulo, Brazil*
[d] *Departamento de Engenharia Metalúrgica e de Materiais, Universidade Federal Do Ceará, Fortaleza, CE, Brazil*
[e] *Grupo de Eletroquímica e Corrosão (GELCORR), Departamento de Química Analítica e Físico-Química, Universidade Federal Do Ceará – UFC, Campus Do Pici, CP 12100, CEP 60451-970, Fortaleza, CE, Brazil*

ARTICLE INFO

ABSTRACT

$Ni_{0.5}Zn_{0.5}Fe_2O_4$ nanocrystals were successfully synthesized under different pure hydrothermal conditions (no organic solvent). The effects of the NaOH content and reaction time on the growth mechanism, as well as structural, morphological and magnetic properties were investigated. High-resolution electron microscopy transmission (HRTEM) revealed the formation of the nanocrystals, mainly via oriented attachment or in addition by a coalescence mechanism depending on the NaOH concentration (3.7 −5.2 M). This secondary mechanism was found to give rise to defects in the network and structural disorder on the surface of the nanocrystals. By extending the reaction time (6−24 h), a morphology transition from truncated-hexagonal to rounded structures was seen, which evidenced a self-integration mechanism to achieve the most stable shape. Moreover, preferential exposure of the (111) plane was observed. Electrochemical measurements using $[Fe(CN)_6]^{3-/4-}$ to check the surface status further supported this statement. This indicated an adsorption effect of the NaOH on the surface of the MNPs allowing an oriented growth of the nanocrystals. In addition, the blocking temperature (T_B) was affected by different factors (rearrangement of the atoms on the surface or increase of the magnetically-ordered core) depending on the hydrothermal conditions used.

© 2017 Elsevier B.V. All rights reserved.

1. Introduction

Magnetic nanoparticles (MNPs) are a class of materials frequently used for the development of the nanotechnology in recent years [1]. Their versatility, due to their intrinsic magnetic properties has attracted many researchers worldwide, since it allows MNPs to be applied in many fields of knowledge, such as nanomedicine [2,3], environmental [4], electronic devices [5], among others [6]. For these applications, the most-used materials display a spinel-type structure (STS), which can be described as a cubic close-packed arrangement of oxygen atoms with spatial symmetry group $O_h^7 (Fd3m)$ [7]. The general formula is MFe_2O_4 or $MO.Fe_2O_3$, where M is a divalent metal with positive charge (Ni^{2+}, Mn^{2+}, Zn^{2+}, among others). Once the STS presents octahedral and tetrahedral sites in the unit cell, another representation can also be used in order to reveal the position of the divalent and trivalent cations: $(A)[B]_2O_4$. The parentheses and brackets indicate the metals in the tetrahedral or octahedral sites, respectively. This is useful to predict the magnetic properties of the STS. However, it is well known that these properties are size- and morphology-dependent [8]. Therefore, the STS nanocrystal growth has to be controlled in order to meet the 'special' requirements regarding size distribution, morphology, chemical composition, and crystallinity demanded by each application.

* Corresponding author.
  E-mail address: fechine@ufc.br (P.B.A. Fechine).

In this context, numerous methodologies including coprecipitation [9], sol-gel [10], microemulsion [11], hydrothermal reaction [12], flow injection [13], and others, have been developed. The most common approach to produce nanoparticles (NPs) is coprecipitation, due to its low cost and ease of scale-up. By using this popular method, Faivre et al. [14] observed the growth mechanism of magnetite — an STS of formula Fe_3O_4 frequently used for biomedical applications [15] — in aqueous medium through cryogenic HRTEM. The authors were able to see the rapid agglomeration of disordered primary NPs growing into larger ones, which indicated a coalescence mechanism since there was no preferential crystallographic orientation. Beyond this finding, it is worth mentioning that the coprecipitation process involves higher nanocrystal growth rate. As a consequence, NP size and distribution may not be precisely controlled [16]. To avoid this limitation, additional solvent-controlled approaches can be used to study the mechanism of NP formation. For instance, Niederberger et al. [17] produced Fe_3O_4 nanocrystals from iron(III) acetylacetonate in benzyl alcohol. However, Georg et al. [18] have demonstrated that organic side products are obtained in the mixture during the synthesis through the solvent-controlled route, which affect the nanocrystal growth mechanism. So, reliable results regarding this might not be obtained.

To investigate the formation of NPs, the method to produce the nanocrystals should allow the regulation of the rate and uniformity of nucleation, growth and ageing. In this sense, hydrothermal reactions need to be considered [19]. One of the successful examples is the study performed by Hong et al. [20] where the authors developed a multistep kinetic model in order to explain the growth of ZnS nanocrystals synthesized under different hydrothermal conditions. Later, Lin et al. [21] investigated the growth kinetics of SnO_2 NPs and a growth model of self-integration was proposed. Recently, Wu et al. [22] synthesized hexagonal α-Fe_2O_3 nanorods using an simples double ligand-assisted hydrothermal method and the growth mechanism was elucidated based on the cooperative action of PO_4^{3-} and formamide. Given the exposed, it is noticeable that the hydrothermal treatment is normally used to investigate the nanocrystal growth of different nanomaterials. However, a report emphasizing the growth process of MNPs under pure hydrothermal conditions (no organic solvent) is difficult to find in the literature. Most of the works combined this methodology with other techniques, such as microemulsion [23], or two-phase interfacial reaction [24], among others, which makes the synthetic process expensive due to the demand of additional purification steps of the final product. Taking this context into account, we have investigated the nanocrystal growth of $Ni_{0.5}Zn_{0.5}Fe_2O_4$ — a versatile STS with high saturation magnetization and chemical stability [25] — synthesized under different pure hydrothermal conditions. The roles of reaction time and NaOH content were studied and high resolution transmission electron microscopy (HRTEM) strongly suggests oriented attachment (OA) [26], an exclusive mechanism to grow the nanocrystals. However, coalescence can take place under high NaOH content, which leads to microstructural defects. Furthermore, superparamagnetic behavior was observed for the MNPs synthesized.

2. Experimental

2.1. Material and methods

The chemical reagents for this study were glacial acetic acid (CH_3CO_2H, Vetec, 99.8%), iron(III) chloride hexahydrate ($FeCl_3.6H_2O$, Dinâmica, 97%), nickel chloride hexahydrate ($NiCl_2.6H_2O$, Vetec, 97%), anhydrous zinc chloride ($ZnCl_2$, Dinâmica,

97%), sodium hydroxide (NaOH, Cinética Química, 97%) and potassium ferrocyanide ($K_4Fe(CN)_6$, 98.5%), potassium ferricyanide ($K_3Fe(CN)_6$, 99%), potassium chloride (KCl, 99%), all from Vetec. CS low molecular weight solution (20–300 cP, 1% w/v in 1% acetic acid). All chemicals were used without further purification.

2.2. Synthesis of $Ni_{0.5}Zn_{0.5}Fe_2O_4$ MNPs

The MNPs were synthesized using the coprecipitation method followed by hydrothermal reaction [7]. Briefly, salt precursors were dissolved at a molar ratio of 0.5:0.5:2 (1.85 mM Ni: 1.85 mM Zn: 7.39 mM Fe) using distilled water previously acidified using 50 μL of acetic acid. Under vigorous mechanical stirring, 10 mL of NaOH (3.0–5.2 M) was added dropwise into the mixture to precipitate the desired hydroxides. The resultant solution was placed in a Teflon-lined autoclave in order to perform the hydrothermal reaction for different times (0.5–24 h) at 250 °C. Afterwards, the product was cooled naturally, filtered and exhaustively washed with distilled water and methanol. Finally, the powder was dried in a muffle furnace at 100 °C for 3 h and stored for characterization. Table 1 shows all the conditions used, as well as the label for each sample. By analyzing the variation of the parameters, it can be seen that samples MNP1–4 were synthesized to study the effect of the NaOH concentration, while samples MNP5 − 7 were obtained to evaluate the influence of the hydrothermal reaction time.

2.3. Characterization of MNPs

2.3.1. Powder X-ray diffraction (PXRD)
The PXRD analysis was obtained using CuKα (1.54056 Å) from a Rigaku X-ray powder diffractometer with Bragg–Brentano geometry in the angular range of 15–85° (2θ). The phase identification analysis was made by comparing powder diffractograms with standard patterns from the International Center for Diffraction Data (ICDD). Rietveld refinement procedures [27] were applied to all diffraction patterns using DBWTools software, version 2.3 [28].

2.3.2. Fourier transform infrared spectroscopy (FT-IR)
FT-IR spectroscopy was carried out on a Perkin–Elmer Spectrometer in the range 4000–400 cm^{-1}. In recording FT-IR spectra, the samples were mixed with potassium bromide powder and pressed into pellets.

2.3.3. ^{57}Fe mössbauer spectroscopy
The Mössbauer spectra were recorded at room temperature (300 K) using a FAST (ConTec) Mössbauer System spectrometer with transmission geometry. A^{57}Co radioactive source was used. The data analysis was performed using the NORMOS program written by R. A. Brand (distributed by Wissenschaftliche Elektronik GmbH, Germany). Isomer shifts (d) are referred as α-Fe at room temperature.

2.3.4. Magnetization measurements
The magnetic measurements were obtained using a vibrating sample magnetometer (Cryogenic VSM 5 T system) with a temperature range 5–300 K. The VSM had been previously calibrated using a pure Ni sphere, and after measuring the mass of each sample the magnetization was given in emu/g.

2.3.5. Electrochemical measurements
Cyclic voltammetry measurements were carried out with a Autolab PGSTAT 101 Metrohn-Eco Chemie, controlled by a personal computer using Nova version 1.11.2 software, and using a conventional three-electrode system, which was composed of a modified

Table 1
Label and set of conditions (NaOH concentration and hydrothermal reaction time) used to identify and to synthesize each sample.

Samples	[NaOH] (mol L^{-1})	time (h)
MNP1	3.0	0.5
MNP2	3.3	0.5
MNP3	4.5	0.5
MNP4	5.2	0.5
MNP5	3.7	6
MNP6	3.7	12
MNP7	3.7	24

glassy carbon electrode (GCE) (0.071 cm^2, BASi) as the working electrode, a Pt sheet as auxiliary electrode and an Ag$_{(s)}$/AgCl$_{(s)}$/Cl$^-_{(aq)}$ (saturated KCl) as reference electrode. All measurements were performed in a solution of 1.0×10^{-3} mol L^{-1} Fe(CN)$_6^{3-/4-}$ containing 0.1 mol L^{-1} KCl at different scan rates. The GCE was carefully polished with 3 μm diamond paste and ultrasonicated in ethanol and purified water. Prior to the modification, the GCE was polished with 3 μm diamond paste slurry, rinsed with ultrapure water, cleaned ultrasonically in ethanol and water alternately for 3 min, and then dried with nitrogen. Next, 5 μL of the prepared MNP suspension (after sonication for 10 min) was dropped on the cleaned GCE surface, and the solvent was allowed to evaporate at a temperature of 60 °C for 15 min. Then, an aliquot (5 μL) of a 0.5% (w/v) CS solution was added and the GCE/MNP returned to 60 °C for another 15 min. When not in use, the sensor was stored in a desiccator.

2.3.6. Transmission electron microscopy (TEM)

The TEM images were obtained with a MSC JEOL TEM-2100 200 kV microscope, equipped with a CCD (TVip−16 MP) and TV (Gatan ES500W) available from LNNano, Campinas, Brazil. TEM samples were dispersed in isopropyl alcohol and deposited in a drop onto carbon-coated copper grids. Subsequently, the deposited samples were allowed to dry completely overnight before examination.

3. Results and discussion

PXRD patterns for all samples synthesized in this work are shown in Fig. 1(a). The black dots denote the observed data (Obs), while the red and blue lines represent the calculated data (Cal) and the difference (Dif) between the data, i.e. Obs − Calc, respectively. It was possible to see the main diffraction peaks at 30.1°, 35.4°, 43.1°, 53.4°, 57.0°, 62.5°, 74.1° and 89.7° for all samples. Clearly, the patterns indicate the formation of the spinel structure through hydrothermal reaction under different conditions. Furthermore, the fit of the sharp diffraction peaks observed at high angles evidences good crystallinity [29,30]. Broad diffraction peaks were found for samples MNP1−2, suggesting an amorphous structure. Since the amount of NaOH was sufficient stoichiometrically to carry out the crystallization process, explanations related to that were discarded. Thus, the amorphous structure may be caused by interference by chemical species, which might inhibit the formation of the spinel structure [31]. Moreover, it is worth mentioning that small NP size could also explain the observed amorphous behavior [32].

To further investigate the structural features, Rietveld refinement was performed for samples MNP3−7. As a result, parameters such as average crystallite size (D), microstrain (ε) and network parameters were obtained. Table 2 summarizes these data, as well as the weighted profile R-factor (R_{wp}) and the goodness of fit index (χ^2) values, which can be utilized to verify the agreement between experimental and calculated data. In this regard, it is important to know that the smallest value that R_{wp} can reach is the expected R-factor (R_{exp}) and that χ^2 should never drop below one [33], since this parameter is obtained by using the following relationship:

$$\chi^2 = \frac{R_{wp}}{R_{exp}} \tag{1}$$

Therefore, once the refinement process starts, the value of χ^2 should approach unity so long as the convergence between the data improves. Given this knowledge, the values for R_{wp} and χ^2 displayed in Table 2 indicate the goodness of the Rietveld refinement carried out for MNP3−7. Additionally, similar results can be found in the literature [34]. So, in the present case, the calculated nanocrystal structure for these samples can be regarded as satisfactory. The Rietveld method was not performed for MNP1−2, since an amorphous nature was observed in the PXRD measurements.

By using the refined data, the crystallite size (D) was firstly estimated utilizing the Scherrer equation:

$$D_S = \frac{k\lambda}{\beta \cos\theta} \tag{2}$$

where k is the shape coefficient for the reciprocal lattice point, λ is the wavelength of the incident radiation, β is the full width at half-maximum (FWHM) of the diffraction peak and θ is the Bragg angle. However, it is well known in the literature [35] that the β values for the observed diffraction peaks can be described assuming different contributions from instrumental effects, D and microstrain (ε), i.e.

$$\beta = \beta_{inst} + \beta_D + \beta_\varepsilon \tag{3}$$

Therefore, it is apparent that the β value needs to be corrected in order to obtain accurate values for D_S. In this sense, the Rietveld method helps to eliminate the β_{inst} by introducing data in the model from a standard sample [36]. The additional line broadening of the diffraction peak due to ε can be eliminated using the Williamson-Hall (WH) plot, which assumes the β value to be the sum of β_D and β_ε. In this case, D_{WH} and ε are calculated using the WH equation [37]:

$$\frac{\beta}{\lambda}\cos\theta = \frac{k}{D_{WH}} + \frac{4\varepsilon}{\lambda}sen\theta \tag{4}$$

The D_S, D_{WH} and ε values obtained are presented in Table 2. For samples MNP3−4, it was possible to observe an increase in size as a function of the NaOH concentration. The ε values for the samples MNP3−4 were 0.212 and 0.276%, respectively. Once this parameter directly reveals the deformation of the crystal lattice [38], these results may indicate poor nanocrystals growth under high NaOH concentration.

The MNP4 heterogeneity can also be checked by analyzing the D values obtained through different equations. The calculated D_S and D_{WH} values for MNP4 were 18.8 and 49.2 nm, respectively, which gives a difference ($D_{WH}-D_S$) of 30.4 nm. This discrepancy is easily explained by examining the corrections performed to calculate the D values. In order to estimate D_S, the β parameter was firstly corrected to eliminate the contribution from instrumental effects using a standard sample. However, the β value extracted from Rietveld refinement neglects the contribution of ε to the width of the diffraction peaks. Therefore, if ε is large, the D values estimated through Eq. (2), the so-called Scherrer formula, may provide a rough approximation. On the other hand, the Williamson-Hall plot supposes the contribution of D and ε to the width of diffraction peaks. Thus, upon instrumental correction, the calculated D values using Eq. (4) may be more accurate. However, it is important to
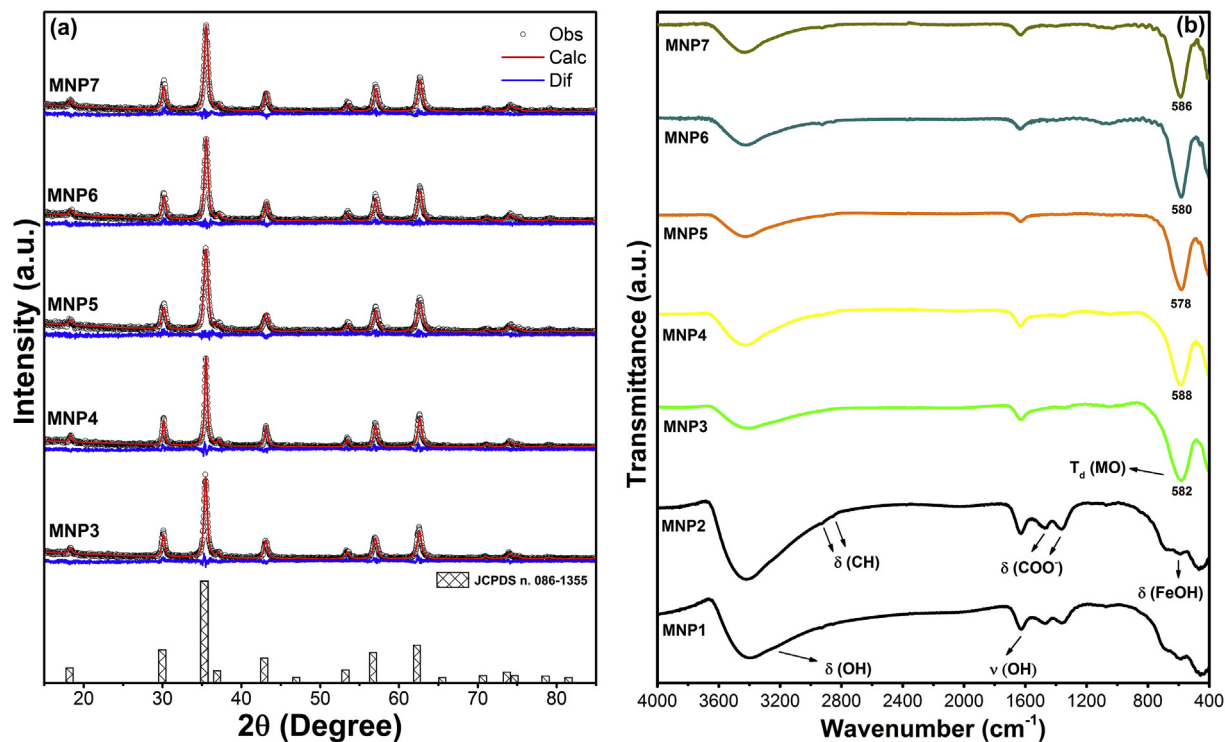
Fig. 1. (a) PXRD patterns for MNP3–7 taken at room temperature. Observed and calculated data are denoted by unfilled circles and red lines, respectively. The calculated data was obtained through the Rietveld method and the blue line under each pattern denotes the difference between experimental and calculated data. The patterned columns correspond to the spinel phase standard number 086–1355 obtained from the Joint Committee on Powder Diffraction Standards (JCPDS). (b) FT-IR spectrum for MNP1–7. (For interpretation of the references to color in this figure legend, the reader is referred to the Web version of this article.)

Table 2
Values of average crystallite size (D), microstrain (ε), network parameter, R_{wp} and S for the samples that showed spinel phase.

Samples	D_S (nm)	D_{WH} (nm)	ε (%)	Network Parameter (Å)	R_{wp} (%)	χ^2
MNP3	15.8	27.9	0.212	8.3901	15.27	1.14
MNP4	18.8	49.2	0.276	8.3881	15.86	1.17
MNP5	13.3	16.8	0.127	8.3805	15.65	1.14
MNP6	15.5	20.3	0.127	8.3843	16.71	1.19
MNP7	15.8	20.0	0.142	8.3805	15.71	1.16

mention that this is true when the ε parameter is found to be large, which strongly evidences the structural heterogeneity of the sample studied. In contrast, if the ε contribution is irrelevant to the peak broadening, D_S and D_{WH} values should be similar. For MNP4, it was possible to notice the largest difference between the D values estimated by the Scherrer formula and the Williamson-Hall plot. So, this indicates a large contribution of ε to the β value, which can be attributed to the structural heterogeneity of the synthesized nanocrystal under the highest NaOH concentration. In addition, the lattice parameters for MNP3–4 were found to be 8.3901 and 8.3881 Å, respectively. The lattice shrinkage may be attributed to the cationic mobility between the tetrahedral and octahedral sites in order to decrease ε at the lattice site.

For MNP5–7, the D values obtained through different equations ranged from 13.3 to 20.0 nm. In this case, the discrepancy between D_S and D_{WH} values are smaller, which indicates a low contribution of ε to the width of diffraction peaks. This is further supported by the data in Table 2, since the Williamson-Hall method gave ε values of 0.127, 0.127 and 0.142% for MNP5–7, respectively. Furthermore, it reveals a nanocrystal containing less imperfection and distortion. Interestingly, the lattice parameters for these samples were found

to have no regular behavior. However, for MNP6–7, a lattice contraction was observed as the value of ε increased, which is the same effect noticed for MNP3–4. Therefore, this lattice behavior seems not to be dependent on the experimental conditions.

Fig. 1(b) shows the FT-IR spectra of the samples. According to the literature [5,39], five normal modes ($5T_{1u}$) can be observed from infrared crystal lattice vibration. In the range studied ($4000–400\ cm^{-1}$), only two modes related to octahedral and tetrahedral sites can be seen below $700\ cm^{-1}$. No bands related to spinel phase were observed for MNP1–2, which evidences an amorphous nature, in agreement with PXRD data. The presence of bands at 3500 and $1500\ cm^{-1}$ can be attributed to the stretch and bend vibrations of the O–H group, respectively. For both MNP1–2, a band observed at $592\ cm^{-1}$ is characteristic of Fe–OH stretch [40]. Clearly, these results suggest the presence of intermediate species. Interestingly, bands related to the C–O and C–H species adsorbed on the surface of the MNPs were found for both MNP1–2. Also, bands observed in the range $1500–1300\ cm^{-1}$ are correlated to COO^- [41]. It was also possible to observe the presence of bands at 2921 and $2855\ cm^{-1}$. These bands can be attributed to the vibrations of C–H stretch from alkane species, which indicates acetate ions adsorbed on the surface of MNP1–2. Once these samples had shown amorphous structure according to the PXRD, it is fair to infer that the acetate ions on the surface of the MNPs may act as protecting agents inhibiting the crystallization process. Similar results were observed by Nagase et al. [42].

For MNP3–7, bands related to the tetrahedral site (symmetry T_d) from spinel phase were clearly found in the range from 576 to $586\ cm^{-1}$ [43]. Once again, this is in agreement with the PXRD data. The slight discrepancy between the positions of the bands may be due to cationic mobility under different experimental conditions [44]. Another band observed close to $400\ cm^{-1}$ is assigned to the

'octahedral' site (symmetry D_{3d}). Further, bands from O–H stretch and bend from hydroxyl groups attached to the MNP surface were seen at 3500 and 1500 cm^{-1}, respectively. However, it is important to mention that water molecules adsorbed on the surface can also contribute to these bands [45].

Fig. 2 shows the typical Mössbauer spectra for MNP3–7 recorded at room temperature. The experimental data points are represented by the black dots, while the solid red line coincides with least-square fitting. Solid lines with different colors denote the adjustment performed. Many sub-spectra (blue, green, yellow, pink and cyan) were found. Thus, it is possible to infer that iron is located in sites with different magnetic neighborhoods. A central doublet peak was observed only for MNP3. This can be attributed to superparamagnetic behavior arising from collapse of the magnetic ordering due to small particle size [46,47]. On the other hand, a paramagnetic doublet can also appear due to interaction between Fe^{3+} and non-magnetic Zn^{2+} ions [48]. For all samples, a single peak pattern was observed. This V-shaped peak may be assigned to the reduction of the magneto-crystalline anisotropy or insertion of zinc in the spinel structure, which reduces the magnetic interactions between sites by decreasing the A–B coupling pairs [49]. In order to obtain a satisfactory fit to describe the ferromagnetic nature of the samples, a high number of sextet patterns were required. This can be explained by the variety of cations in the sample (Zn^{2+}, Ni^{2+} and Fe^{3+}) as well as their preference for site occupation. It is well known that $ZnFe_2O_4$ is a normal spinel structure in which Zn^{2+}(diamagnetic) has high preference for tetrahedral sites [50]. On the other hand, $NiFe_2O_4$ is an inverse spinel structure where Ni^{2+} (paramagnetic) occupies octahedral positions [51]. Therefore, the distribution of the diamagnetic (Zn^{2+}) and paramagnetic (Ni^{2+} and Fe^{3+}) cations leads to different magnetic neighborhoods. Since distinct combinations like Fe-O-Fe, Fe-O-Ni and/or Fe-O-Zn might be found, even considering the preferential occupation of the studied ions. This explains the many sub-spectra necessary to obtain an acceptable fit model for tetrahedral A-site and octahedral B-site. Another plausible explanation for the multi-sextet fit is the presence of canted spins as suggested by Yafet and Kittel [52].

The hyperfine parameters obtained are showed in Table 3. The range of isomer shift (δ) values found (0.29–0.39 mm/s) indicate a high-spin Fe^{3+}state [48]. The parameter δ is related to the electrostatic interaction between s-electrons with a finite probability to be found close to the nucleus, as well as the charge distribution surrounding it. In other words, the change in this parameter can be interpreted as the difference in the Fe^{3+}–O–Fe^{3+} inter-nuclear separation, which is normally larger for octahedral B-site ions as compared to that for tetrahedral A-site ions [53]. Therefore, the greater overlapping of orbitals of Fe^{3+} and O^{2-} ions found for the tetrahedral A-sites will result in a higher covalency and hence smaller δ values. The δ values obtained in this work shown no appreciable changes under different experimental conditions. For the quadrupole interaction (Δ), most values were observed in the range of -0.06 to $+0.06$ mm/s. This shows a weak influence of the experimental conditions on the parameter Δ. However, a doublet with Δ equal to 1.20 mm/s was found only for MNP3. Non-zero Δ values denote the presence of an electric field gradient (EFG) arising from chemical disorder in the spinel structure [54]. Thus, a large local symmetry reduction in site was observed for MNP3. In addition to the hyperfine parameters, the hyperfine magnetic field (B_{HF}) and percentage area can be used to assign the sub-spectrum to a specific configuration (octahedral B-site or tetrahedral A-site). Based on these parameters, the assignment for each sub-spectrum fitted can be seen in Table 3.

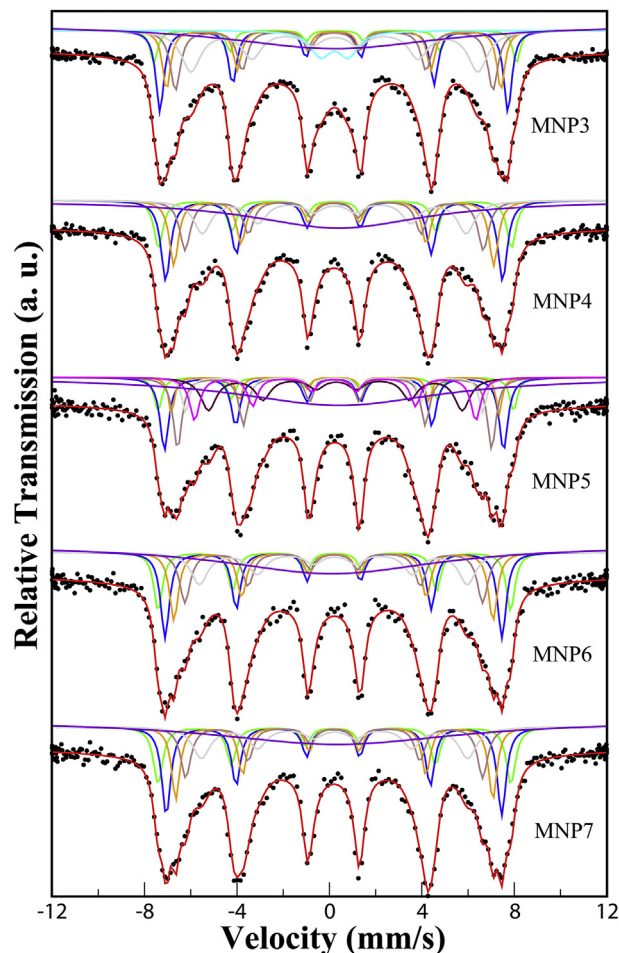The average crystallite size from low-magnification TEM

Fig. 2. Mössbauer spectra for MNP3–7. The black points denote the experimental data and the red line corresponds to the sum of the different sub-spectra represented by purple, green, blue, yellow, brown and gray lines. (For interpretation of the references to color in this figure legend, the reader is referred to the Web version of this article.)

micrographs (D_{TEM}) was estimated using 100 MNPs chosen randomly. The distribution graphs for MNP3–7 are shown in Fig. 3. A normal distribution was used to fit the data. The D_{TEM} values found for MNP3–7 were 16.4 ± 4.4, 29.5 ± 6.8, 14.8 ± 2.9, 14.7 ± 2.5 and 14.9 ± 3.9, respectively. These results are in good agreement with the PXRD data for MNP3 and MNP5–7. For MNP4, the D_{TEM} value was found to have a relevant discrepancy if compared to the D_S and D_{WH} values (See Table 2). Once the largest ε was observed for MNP4, the disagreement can be explained by the nanocrystal imperfections due to the poor growth under high NaOH concentration. TEM observations for MNP3–4 revealed greater D_{TEM} values with increase in NaOH concentration. In order to explain this, it is worth mentioning that the literature has reported NaOH to have a strong adsorption effect capable of slowing down the dissolution of the NPs, which makes the solution being far from saturated [20]. Also, the effect mentioned was found to be even greater under hydrothermal conditions [55]. Therefore, the nanocrystal growth was considered to occur exclusively via OA [56], since the Ostwald ripening (OR) mechanism [57–59] is thermodynamically prohibited in an unsaturated solution. The OA mechanism is based on the attachment of two crystallographically oriented NPs to form a larger one. However, the growth rate for the pure OA-based mechanism seems to increase with increase in the NaOH concentration, which can be explained by the interaction

Table 3
Mössbauer parameters for samples MNP3–7.

| Samples	Sites	Hyperfine parameters			Area (%)
		δ (mm/s)	Δ (mm/s)	B_{HF} (T)	
MNP3	A_0	0.29	0.02	46.7	15.0
	A_1	0.30	−0.02	44.9	11.0
	A_2	031	0.00	42.6	14.0
	B_0	0.35	0.00	48.6	5.60
	B_1	0.34	−0.03	38.5	18.0
	B_2	0.33	1,20	−	5.60
	B_3	0.36	−	−	30.8
MNP4	A_0	0.31	0.02	45.2	18.5
	A_1	0.30	−0.02	42.9	14.5
	B_0	0.33	−0.02	40.0	13.0
	B_1	0.33	0.04	47.3	10.5
	B_2	0.32	−0.01	35.4	13.7
	B_3	0.50	−	−	29.8
MNP5	A_0	0.30	0.00	45.5	14.6
	A_1	0.33	0.06	44.0	4.8
	A_2	0.33	−0.01	42.0	14.2
	A_3	0.34	−0.04	39.8	5.9
	B_0	0.39	−0.03	34.0	11.5
	B_1	0.34	0.05	37.7	9.8
	B_2	0.54	−	−	33.3
	B_3	0.35	0.06	47.7	5.9
MNP6	A_0	0.22	−	−	35.0
	A_1	0.29	−0.01	45.2	14.6
	B_0	0.30	−0.02	42.8	4.8
	B_1	0.31	−0.02	39.9	11.9
	B_2	0.32	−0.06	35.9	11.8
	B_3	0.34	0.00	47.3	11.2
MNP7	A_0	0.29	0.03	45.0	17.5
	A_1	0.32	0.01	42.5	39.8
	A_2	0.31	0.01	39.8	11.6
	B_0	0.33	−0.01	35.7	12.0
	B_1	0.31	0.04	47.3	11.9
	B_2	0.43	−	−	33.4

between the nucleation (formation of crystallization center) and the NPs growth processes [60]. The crystal growth is more efficient at high concentration due to the shift of the equilibrium towards hydrolysis and condensation reactions. Growth prevails against the nucleation, which leads to a small number of large particles. As a result, greater D values can be achieved under the same hydrothermal reaction time condition. This explains why the D_{TEM} value for MNP4 (29.5 ± 6.8 nm) was higher than that observed for MNP3 (16.4 ± 4.4 nm). On the other hand, for MNP5–7, the D_{TEM} values remained statistically equal. Thus, no significant nanocrystal growth was observed by changing the hydrothermal reaction time from 6 to 24 h. This indicates that OR is not an important mechanism in growing the nanocrystals [61], since the general equation considered for these cases according to OR mechanism can be written as:

$$D^n - D_0^n = k \cdot (t - t_0) \qquad (5)$$

where D and D_0 are the average crystallite size at time t and t_0, respectively, k is a temperature-dependent material constant, and n is an exponent relevant to the mechanism. By analyzing Eq. (5), it is easy to see a directly proportional relationship between D and t. Once D_{TEM} values were found to not increase over time, an irrelevant contribution of the OR mechanism to the nanocrystal growth is evidenced. Also, this demonstrates a strong NaOH adsorption effect on the surface of the MNPs, which was able to hinder the OR mechanism over different time periods (6, 12 and 24 h).

The morphological evaluation was also carried out based on high-magnification TEM images. Square-like structures can be seen in Fig. 4(a) and (b) for MNP3 and MNP4, respectively. In order to explain this result, it is important to highlight that nanocrystal shape is governed mainly by different relative plane growth rates. Generally, for a face-center cubic (fcc), such as the spinel phase, the square-like structure is observed when the crystal growth rate along the <111> is faster than the <100> directions [62]. To further support this, the interplanar spacing observed for MNP3 in Fig. S1(a) was measured to be 0.46 nm for both nanocrystals. According to the literature [63], this value can be assigned to the (111) plane of the spinel structure. Therefore, NaOH adsorption effect on the surface of the MNPs caused a preferential decrease in the effective interfacial free energy of the mentioned plane increasing the growth rate. However, the increase of the NaOH concentration did not affect the morphology, since square-like structures can still be observed for both MNP3 and MNP4 in Fig. 4(a) and (b), respectively. This indicates that the preferential adsorption effect is independent of NaOH content under hydrothermal conditions. In addition, these samples possessed a surface roughness pattern, which appeared to be higher for MNP4. This evidences the formation of the MNPs through primary-NP aggregation (Fig. 4(c)), which points to a secondary coalescence mechanism under high NaOH content. Fig. 4(d), which fits part of Fig. 4(c), displays the nanocrystals growing through two kinds of mechanisms. This is clearly observed in the Fig. S1. Interestingly, MNP3 and MNP4 displayed the greater ε values according to the PXRD data. Therefore, the coalescence mechanism may give rise to the imperfections of the crystal lattice, since there is no crystallographic preference for the attachment [64].

Fig. 5(a),(c) and (d), present HRTEM images for MNP5–7, respectively. Unlike MNP3 and MNP4, truncated/regular hexagonal- and/or quasi-spherical structures were observed. MNPs with irregular geometry, smooth edges and round shape might evidence a nanocrystal growth via both OA and OR mechanisms [20]. However, the contribution of the OR mechanism was not significant, since D_{TEM} values for MNP5–7 (14.8 ± 2.9, 14.7 ± 2.5 and 14.9 ± 3.9, respectively) were found to not increase by extending the hydrothermal reaction time. Therefore, the nanocrystal growth was considered to occur exclusively via an OA mechanism. In order to provide evidence for this assumption, a detailed analysis of Fig. 5(a) was carried out, resulting in Fig. 5(b). Clearly, an attachment of small MNPs to a larger one via common crystallographic orientation can be seen for MNP5, which directly evidences the nanocrystal growth through an OA mechanism. Furthermore, a nanocrystal having irregular shape and abrupt edges could also be observed. This further suggests OA as the growth mechanism [65]. For MNP6 and MNP7, a mixture of morphologies was observed. Fig. 5(c) shows the HRTEM image of MNP6. Besides regular hexagonal-like structures, it reveals nanocrystals with round shape and smooth edges. Similar results were observed for MNP7 (Fig. 5(d)), although the number of round-shaped nanocrystals seems to be higher. Thus, after being hydrothermally treated for 24 h at 250 °C, the nanocrystal may change from square to quasi-spherical shape. Given that no growth was observed for MNP5–7, this indicates a rearrangement of the atoms in an attempt to thermodynamically optimize the shape, which additionally supports the nanocrystal growth via an OA mechanism. To explain the observed results for these MNPs, a multistep growth process needs to be adopted. In this context, Lin et al. [21] proposed a model of self-integration during the OA process. In this proposal, the nanocrystal has to undergo three states (A, B and C) to achieve the most stable morphology. States A and B basically denote the combination of two MNPs through common crystallographic orientation, while an atomic mobility is assumed in state C to recrystallize the
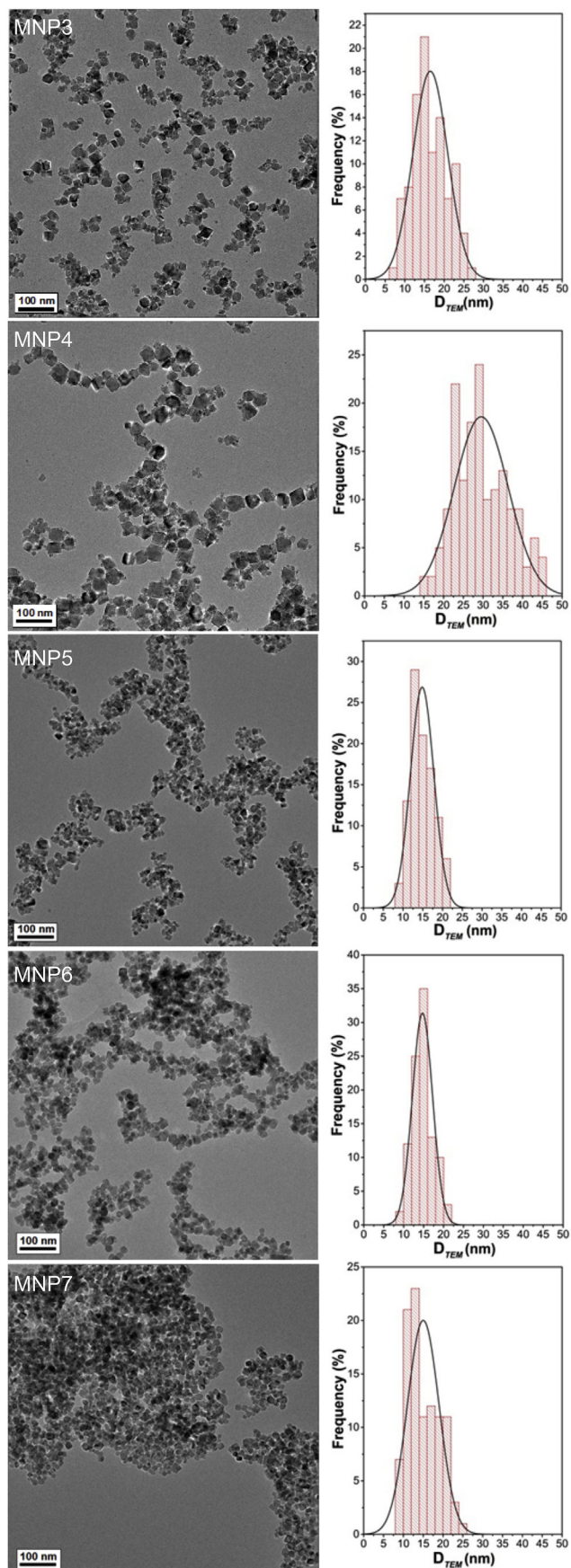
nanocrystal into a round shape. The self-integration effect from A to B is considered to be rapid. Therefore, the visualization of the conjugation of two nanocrystals (state A) is hardly observed, but Fig. 5(b) clearly shows a typical image attributed to state B for MNP5. The rate of self-integration from state B to C is size-dependent. As a consequence, the nanocrystals with different D values may give rise a mixture of distinct shapes when observed after the same period of time. This was observed in Fig. 5(c) and (d) for MNP6 and MNP7, respectively. However, MNP7 displayed a larger number of round-shaped nanocrystals, which indicates self-recrystallization (State C).

In addition to the TEM observations already mentioned, no surface roughness pattern was found for MNP5–7 in Fig. 5(a),(c) and (d), respectively. Therefore, absence of the coalescence mechanism to grow the nanocrystal was observed. This reveals a dependence of the coalescence mechanism on NaOH content. Further, it additionally supports the growth of the MNP5–7 exclusively via an OA mechanism. Given this, the surface structure properties of these MNPs were studied in detail by cyclic voltammetry, since the exposed plane has a great influence on the electrochemical performance of the redox-based electrode materials [66]. The electrochemical evaluation was carried out using $[Fe(CN)_6]^{3-/4-}$ to verify the surface status of the modified electrode [67]. The electrochemical behavior of $[Fe(CN)_6]^{3-/4-}$ is shown in Fig. 6. MNP5/GCE exhibits a pair of redox peaks with the anodic peak potential (E_{pa}) at 0.266 V and the cathodic peak potential (E_{pc}) at 0.191 V. For MNP6/GCE, the E_{pa} and E_{pc} were found to be at 0.270 and 0.207 V, respectively. Analogously, MNP7/GCE presented the E_{pa} at 0.268 V and E_{pc} at 0.195 V. Therefore, the peak-to-peak separation (ΔE_p) values for MNP5–7/GCE were 0.074, 0.063 and 0.073 V, respectively, which indicates a similar electrochemical performance of the MNPs-modified electrodes. Moreover, the cyclic voltammograms of MNP5–7/GCE reveal well-defined symmetric peaks even at different scan rates (υ); meanwhile, I_{pa} and I_{pc} together increase as the square root of the scan rate increases from 10 to 150 mV s^{-1} (see Supporting Information). The peak currents vary linearly with $v^{1/2}$, whose linear regression equations are $I_{pc}(A) = -3.01 \times 10^{-6} + 3.17 \times 10^{-6}v^{1/2}$ (R = 0.9947, n = 6) for MNP5/GCE. For MNP6/GCE, MNP7/GCE and GCE the equations are: $I_{pc}(A) = -2.44 \times 10^{-6} + 3.13 \times 10^{-6}v^{1/2}$ (R = 0.9821, n = 6), $I_{pc}(A) = -2.99 \times 10^{-6} + 2.87 \times 10^{-6}v^{1/2}$ (R = 0.9962, n = 6), and $I_{pc}(A) = -7.93 \times 10^{-7} + 1.82 \times 10^{-6}v^{1/2}$ (R = 0.9997, n = 6) respectively. In order to further deepen the study, the electroactive surface area was calculated according to the Randles-Sevcik equation [68] displayed below:

$$I_p = 2.69 \times 10^5 \, A \, D^{1/2} \, n^{3/2} \, v^{1/2} \, C \tag{6}$$

where A is the electrode area, D is the diffusion coefficient (at 25 °C, $D = 7.60 \times 10^{-6}$ cm^2 s^{-1}), n is the number of electrons transferred in the redox reaction ($n = 1$), C is the concentration of the reactant (1 mM Fe(CN)$_6^{3-/4-}$), I_p refers to the redox peak current and v is the scan rate of the cyclic voltammetry measurement. $I_{pc}v^{-1/2}$ indicated that the modified electrodes possess a larger electro-active surface area compared to that of the bare glassy carbon electrode ($2.45 \times 10^{-3} \pm 1.54 \times 10^{-4}$ cm^2). The values obtained through Eq. (6) were $4.27 \times 10^{-3} \pm 7.91 \times 10^{-4}$ cm^2, $4.22 \times 10^{-3} \pm 3.65 \times 10^{-4}$ cm^2 and $3.39 \times 10^{-3} \pm 7.26 \times 10^{-4}$ cm^2 for MNP5–7/GCE, respectively. Statistically, the electroactive area remained similar. However, it is possible to observe that the

Fig. 3. Low-resolution TEM micrographs and average crystallite size distribution of the MNPs. The distribution graph was created using 100 MNPs chosen randomly and the data was fitted using a normal distribution.
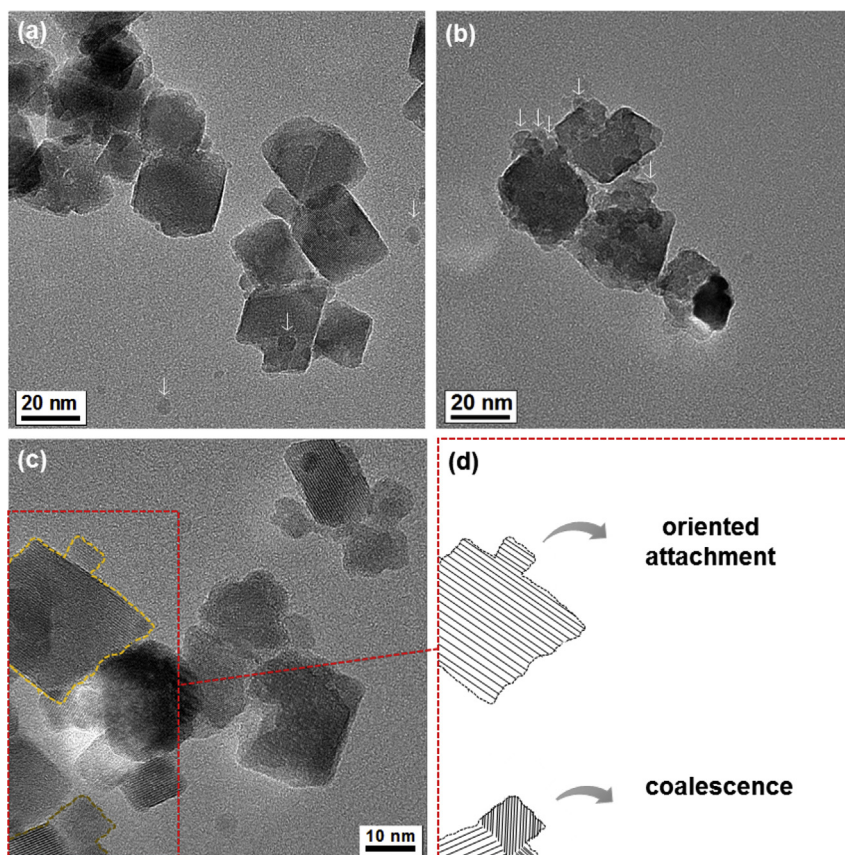
Fig. 4. HRTEM images of (a) MNP3 and (b) MNP4. The arrows point to primary NPs used to grow the nanocrystals through coalescence. A further HRTEM micrograph for MNP3 (c) showing dotted lines indicates nanocrystals growing via different mechanisms. Illustration (d) presents the crystal fringes of the different nanocrystals involved in the OA and coalescence growth mechanism.

electroactive area for the modified electrode was 1.61 times higher than the bare GCE. Taken together, the electrochemical results clearly suggest a similar behavior of the MNP-modified electrodes, which reveals MNP5–7 to have characteristic active surface structure. This further supports the exposure of the (111) plane on the MNPs surface as observed in Fig. 4(c).

Fig. 7(a) shows the magnetization measurements at room temperature for MNP3–7. As can be seen in Fig. 7(b), negligible hysteresis was observed. This evidences a superparamagnetic nature [69]. Interestingly, the Mössbauer spectroscopy showed a ferromagnetic behavior. This difference is due to the relaxation time of the MNPs (τ_{MNP}) as well as the measurement time (τ_m) [47]. Usually, the measurement times for VSM and Mössbauer spectroscopy are 100 and 1×10^{-8} s, respectively. For magnetization measurements performed in this work, the τ_m was much larger than τ_{MNP}. Thus, the MNPs had enough time to reach thermodynamic equilibrium and the superparamagnetic behavior can be observed. In this case, τ_m is smaller than τ_{MNP} for the Mössbauer spectroscopy and the relaxation process is very slow compared to the measurement time. An ordered magnetic system could be achieved and the MNPs were in the so-called blocked regime. Therefore, the ferromagnetic nature was revealed.

The superparamagnetic loops found for the samples at 300 K were well described using the Langevin function (see Supporting Information),

$$\frac{M}{M_0} = \coth\left(\frac{mH}{k_BT}\right) - \frac{k_BT}{mH} \tag{7}$$

where m is the magnetic moment, H is the external magnetic field, T is the temperature, and k_B is the Boltzmann constant. The average crystallite size can be easily correlated with the magnetic properties of the MNPs using this function [7,47,70,71]. Thus, the average crystallite size obtained via Langevin fit (D_L) for MNP3–7 were 13.1, 14.4, 10.7, 14.6 and 12.1 nm, respectively. Moreover, parameters such as saturation magnetization (M_S) can also be obtained from the performed fit. The values found for this parameter were 43.0, 41.2, 44.6, 23.5 and 44.1 emu/g for MNP3–7, respectively. For MNP3–4, a slight decrease of the M_S ($M_S(\Delta) = -1.8$ emu/g=) values was observed. On the other hand, random behavior of M_S values was observed for MNP5–7. The magnetic properties of MNPs can be correlated with several factors, such as composition, D and surface effects, among others. In this case, the composition is the same for all the MNPs studied. Therefore, the factors with strongest effect should be the D and surface effects. No matter the technique used, D was found to increase along with an increase in NaOH concentration. Thus, M_S should be expected to increase. However, a decrease was observed for M_S values for MNP3–4. This highly indicates a strong influence from surface effects. According to the literature [72], the use of NaOH as a precipitant agent can lead to a higher degree of surface disorder compared to alkanolamine bases. Thus, the decrease of M_S may be explained by an increase in the magnitude of the uncompensated spins on the surface. For MNP5–7, D remained similar, but a decrease of M_S value was found for MNP6. Again, the surface effects were playing essential role in the magnetic properties of this sample.

In an attempt to explain the magnetic properties of the MNPs, a core-shell model can be adopted [73]. In this case, a core composed
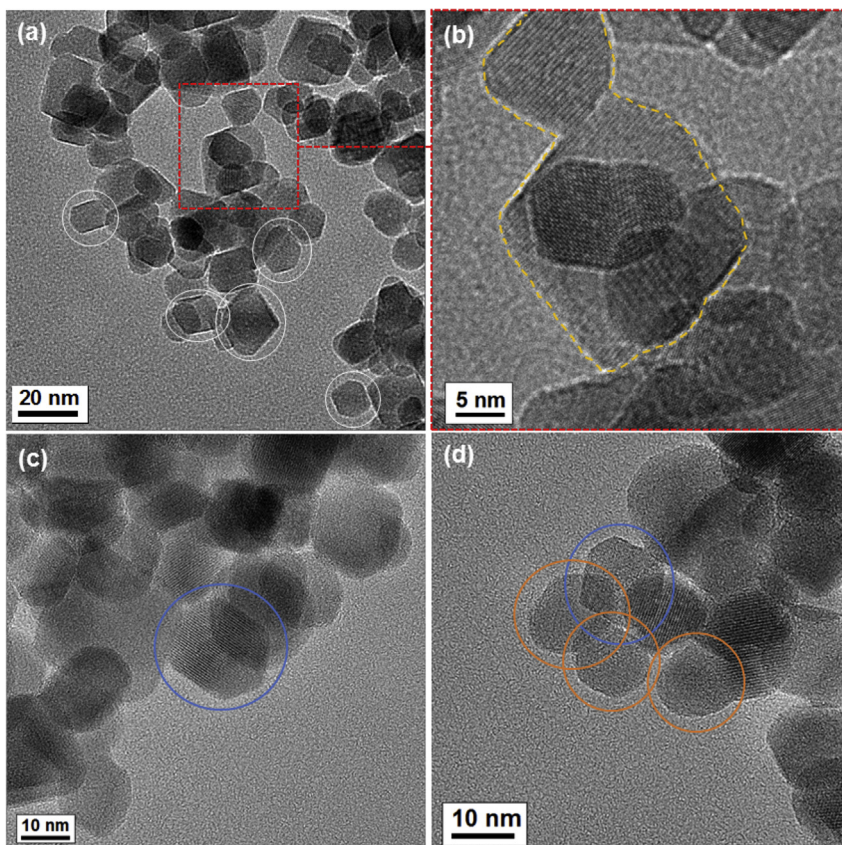
Fig. 5. HRTEM images of (a) MNP5, (b) highlighted MNP5 nanocrystals evidencing the nanocrystal growth through an OA mechanism, (c) MNP6 and (d) MNP7. The red square in (a) denotes the highlighted area of MNP5 in (b). The circles display the different morphologies observed. Truncated and regular hexagonal-like structures are indicated by white and blue circles, respectively, while rounded-shape structures are highlighted by orange circles. (For interpretation of the references to color in this figure legend, the reader is referred to the Web version of this article.)
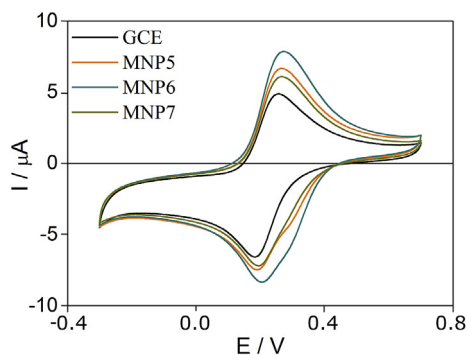
Fig. 6. Cyclic voltammetry of different electrodes in a solution of 1.0×10^{-3} Fe(CN)$_6^{3-/}$ $^{4-}$ and 0.1 mol L^{-1} KCl at a scan rate of 10 mVs^{-1}.

of ordered spins would interact with a magnetically disordered shell ('dead' layer). Thus, the surface effects could strongly influence the magnetic properties of the MNPs. The thickness (t) of the 'dead' layer can be achieved using the following expression,

$$M_S(D) = M_S^{Bulk}\left(1 - \frac{6t}{D}\right) \qquad (8)$$

where $M_S(D)$ is the magnetization saturation related to D and M_S^{Bulk} is the magnetization saturation for the bulk. Assuming D_{TEM} and M_S^{Bulk} equal to 86 emu/g [74], the t values were 1.30, 2.56, 1.18, 1.78

and 1.20 nm for MNP3–7, respectively. These values perfectly explain the change of observed M_S values. For MNP3–4, the increase of t displayed a strong effect on M_S, which may be related to the coalescence mechanism observed under high NaOH concentration, since no crystallographic orientation is required for the nanocrystal growth. On the other hand, t values for MNP5–7 were found to follow a random behavior with the hydrothermal reaction time. This might be related to the shape transition observed through HRTEM images.

Additionally, it is well known that the superparamagnetic behavior observed is strongly related to the critical diameter (D_C) considering a spherical particle model [75]. MNPs with D smaller than D_C exhibit superparamagnetic relaxation. In contrast, MNPs with D larger than D_C display ferromagnetic behavior. According to the literature [76], the D_C value for Ni-Zn ferrite is 21.62 nm. Thus, a blocked regime should be expected for MNP4, since D values were found to be larger than D_C assuming D_{WH} or D_{TEM}. Interestingly, MNP3–7 displayed superparamagnetic character according to the VSM data. This strongly suggests that the D_L or D_S values should be the more accurate parameters to evaluate the MNP regime. The probable reason for this can be found in fundamental concepts about the techniques employed to calculate D values. D_S considers only the crystalline portion of the MNPs. Therefore, the calculated size should be close to that of the magnetically ordered core. D_{WH} can be affected by defects on the surface, which cause a large deviation, as observed for MNP4. D_{TEM} exhibited some difference compared to D_S due to consideration of both crystalline and amorphous portion. D_L was very precise in evaluating the MNPs regime. The Langevin function considers an ideal system where the
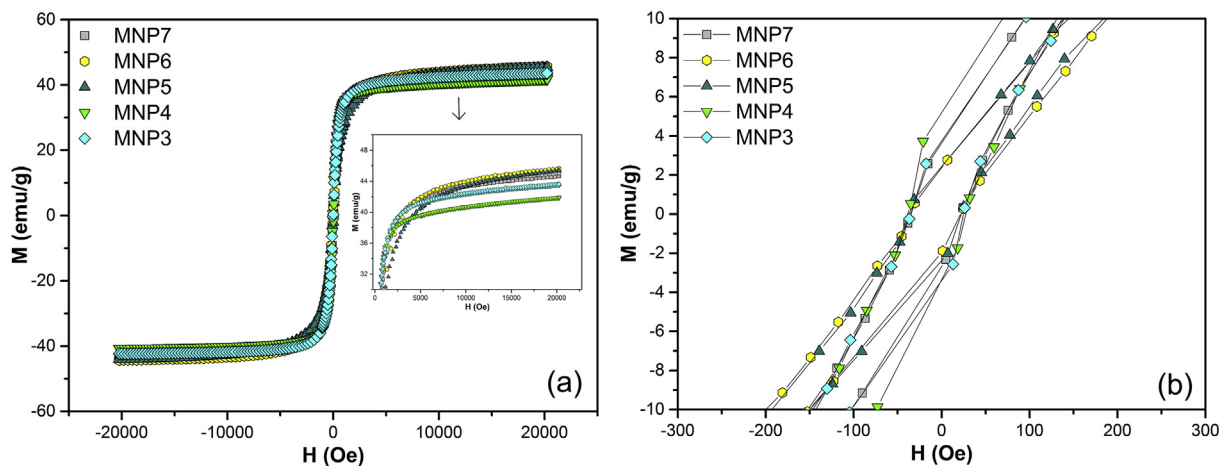
Fig. 7. VSM measurement at room temperature for MNP3–7. (a) Magnetic hysteresis loops and (b) a detailed view of the hysteresis. The inset in the Fig. 7(a) presents a zoom of the magnetic curves for MNP3-7. Specifically, the magnetization data is displayed for values higher than 30 emu/g.

MNPs are non-interacting and spherical [47]. Once HRTEM micrographs for MNP5–7 presented a shape transition from truncated hexagonal-like to quasi-spherical structures, some deviation should be expected. Surprisingly, the parameters obtained using the Langevin fit were found to be in good agreement.

The zero field-cooled (ZFC)/field-cooled (FC) curves at an applied field of 500 kOe for MNP3–7 are shown in Fig. 8. From these experiments, it is possible to find the blocking temperature (T_B). The temperature found can be correlated to the MNP characteristics by the Stoner–Wohlfarth relation [47],

$$T_B = \frac{K_{eff}V_0}{25K_B} \tag{9}$$

where K_{eff} is the average value of the magnetic anisotropy constant, V_0 is volume of the MNP and K_B is Boltzmann's constant. Clearly, a broad distribution of the ZFC curve for each sample can be seen and

the maximum could be denoted as the blocking temperature (T_B). However, it is important to remember the wide profile found for the ZFC curve can be understood as a distribution of different T_B values for various NP crystallite sizes. Therefore, the maximum observed denotes a mean. In this sense, a better way to represent this parameter is T_B^m. For the samples synthesized in this work, the values found for T_B^m were 105, 121, 103, 137 and 153 K for MNP3–7, respectively. From Eq. (6), these values can be correlated with MNP characteristics. Thus, it is possible to see that an increase both in NaOH concentration and in hydrothermal reaction time led to larger values of T_B^m. Although the effect seems to be similar, the source for the two set of samples may be different. For MNP3–4, an increase in crystallite size was observed by increasing the NaOH concentration. Thus, the T_B^m values found for these samples can be easily explained by the increase in V_0. In contrast, a similar crystallite size was achieved for MNP5–7, which indicates a negligible contribution of V_0. In this way, K_{eff} should make a large
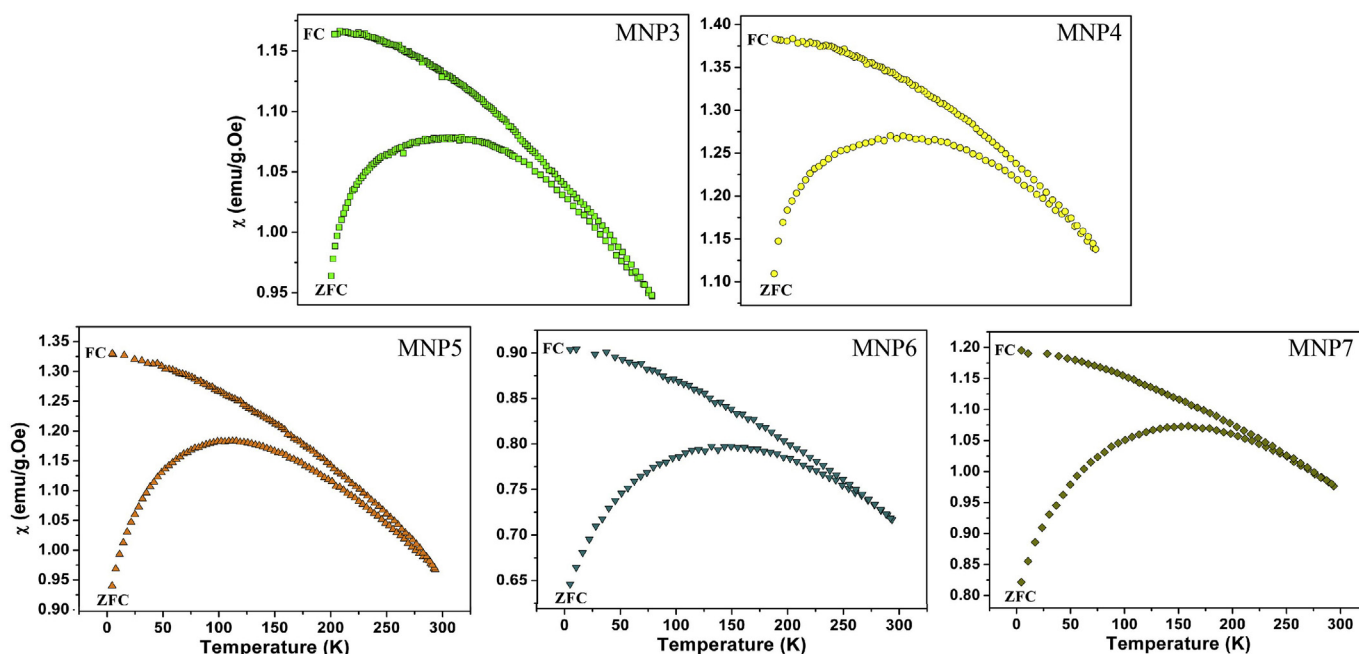

Fig. 8. ZFC/FC measurements for MNP3–7 using an applied field of 500 kOe.

contribution to the increase of T_B^m with hydrothermal reaction time. This can be related to the shape transition observed in the HRTEM images for MNP5–7 (see Fig. 5(a), (c) and (d)). The change of morphology would increase K_{eff} leading to higher values of T_B^m. Additionally, thermomagnetic irreversibility for each sample was observed from the temperature where the ZFC and FC curves superimpose. According to the literature [44], this behavior is characteristic of the superparamagnetic regime of the NPs synthesized, as well as spin-glass-like states.

4. Conclusion

The growth of $Ni_{0.5}Zn_{0.5}Fe_2O_4$ nanocrystals, as well as their structural, morphological and magnetic properties has been successfully investigated under different pure hydrothermal conditions. The role of NaOH content and reaction time was studied. MNPs grew exclusively through an OA mechanism in alkaline aqueous solution. However, a secondary coalescence mechanism acts under strongly alkaline conditions, which leads to lattice deformations and an increase of the spin-disordered surface layer, affecting the magnetic properties. Furthermore, NaOH was found to have a very strong adsorption effect capable of hindering the OR mechanism and preferentially exposing the (111) plane on the surface of the nanocrystals. HRTEM images and electrochemical measurements confirmed the exposure of this plane. By extending the reaction time, a morphology transition in order to achieve the most stable shape was observed. MNPs were found to change from truncated-hexagonal to rounded structures after 24 h, which can be explained by a self-integration mechanism. Furthermore, T_B appeared to be affected by different structural factors. Under high NaOH content conditions, the size of the magnetically-ordered core was found to have a predominant effect on T_B values. However, surface effects played an essential role increasing the reaction time, which may be associated with a rearrangement of the atoms on the surface of the MNPs due to the morphology transition.

Appendix A. Supplementary data

Supplementary data related to this article can be found at https://doi.org/10.1016/j.jallcom.2017.12.088.

References

[1] A. Akbarzadeh, M. Samiei, S. Davaran, Magnetic nanoparticles: preparation, physical properties, and applications in biomedicine, Nanoscale Res. Lett. 7 (2012), 144–144.

[2] S.R. Dave, X. Gao, Monodisperse magnetic nanoparticles for biodetection, imaging, and drug delivery: a versatile and evolving technology, Wiley Interdisc. Rev. Nanomed. Nanobiotechnol. 1 (2009) 583–609.

[3] A. Barreto, V. Santiago, R. Freire, S. Mazzetto, J. Denardin, G. Mele, I. Cavalcante, M. Ribeiro, N. Ricardo, T. Gonçalves, L. Carbone, T. Lemos, O. Pessoa, P. Fechine, Magnetic nanosystem for cancer therapy using onco-calyxone A, an antitomour secondary metabolite isolated from a brazilian plant, Int. J. Mol. Sci. 14 (2013), 18269–18269.

[4] S.C.N. Tang, I.M.C. Lo, Magnetic nanoparticles: essential factors for sustainable environmental applications, Water Res. 47 (2013) 2613–2632.

[5] R.M. Freire, P.G.C. Freitas, T.S. Ribeiro, I.F. Vasconcelos, J.C. Denardin, G. Mele, L. Carbone, S.E. Mazzetto, P.B.A. Fechine, Effect of solvent composition on the structural and magnetic properties of MnZn ferrite nanoparticles obtained by hydrothermal synthesis, Microfluid. Nanofluidics (2013) 1–12.

[6] A.H. Latham, M.E. Williams, Controlling transport and chemical functionality of magnetic nanoparticles, Accounts Chem. Res. 41 (2008) 411–420.

[7] R.M. Freire, T.S. Ribeiro, I.F. Vasconcelos, J.C. Denardin, E.B. Barros, G. Mele, L. Carbone, S.E. Mazzetto, P.B.A. Fechine, MZnFe2O4 (M = Ni, Mn) cubic superparamagnetic nanoparticles obtained by hydrothermal synthesis, J. Nanoparticle Res. 15 (2013) 1–12.

[8] Z.X. Tang, C.M. Sorensen, K.J. Klabunde, G.C. Hadjipanayis, Size-dependent magnetic properties of manganese ferrite fine particles, J. Appl. Phys. 69 (1991) 5279–5281.

[9] A.C.H. Barreto, V.R. Santiago, R.M. Freire, S.E. Mazzetto, J.M. Sasaki, I.F. Vasconcelos, J.C. Denardin, G. Mele, L. Carbone, P.B.A. Fechine, Grain size control of the magnetic nanoparticles by solid state route modification, J. Mater. Eng. Perform. 22 (2013) 2073–2079.

[10] Pushpendra Kumar, Pawan Mishra, S.K. Sahu, Synthesis of Ni-Zn ferrites using low temperature sol-gel process, IJSER 2 (2011) 1–4.

[11] A. Košak, D. Makovec, A. Žnidaršič, M. Drofenik, Preparation of MnZn-ferrite with microemulsion technique, J. Eur. Ceram. Soc. 24 (2004) 959–962.

[12] S. Verma, P.A. Joy, Y.B. Khollam, H.S. Potdar, S.B. Deshpande, Synthesis of nanosized MgFe2O4 powders by microwave hydrothermal method, Mater. Lett. 58 (2004) 1092–1095.

[13] G.S. Alvarez, Synthesis, characterisation and applications of iron oxide nanoparticles, in: KTH, Superseded Departments, Materials Science and Engineering, Stockholm University, Stockholm, 2004, p. 67.

[14] J. Baumgartner, A. Dey, P.H.H. Bomans, C. Le Coadou, P. Fratzl, N.A.J.M. Sommerdijk, D. Faivre, Nucleation and growth of magnetite from solution, Nat. Mater. 12 (2013) 310–314.

[15] S. Laurent, D. Forge, M. Port, A. Roch, C. Robic, L. Vander Elst, R.N. Muller, Magnetic iron oxide nanoparticles: synthesis, stabilization, vectorization, physicochemical characterizations, and biological applications, Chem. Rev. 108 (2008) 2064–2110.

[16] L.L. Vatta, R.D. Sanderson, K.R. Koch, An investigation into the potential large-scale continuous magnetite nanoparticle synthesis by high-pressure impinging stream reactors, J. Magn. Magn Mater. 311 (2007) 114–119.

[17] N. Pinna, S. Grancharov, P. Beato, P. Bonville, M. Antonietti, M. Niederberger, Magnetite Nanocrystals: nonaqueous synthesis, characterization, and solubility, Chem. Mater. 17 (2005) 3044–3049.

[18] M. Niederberger, G. Garnweitner, Organic reaction pathways in the nonaqueous synthesis of metal oxide nanoparticles, Chem. Eur J. 12 (2006) 7282–7302.

[19] A. Sachdev, I. Matai, S.U. Kumar, B. Bhushan, P. Dubey, P. Gopinath, A novel one-step synthesis of PEG passivated multicolour fluorescent carbon dots for potential biolabeling application, RSC Adv. 3 (2013) 16958–16961.

[20] J. Zhang, Z. Lin, Y. Lan, G. Ren, D. Chen, F. Huang, M. Hong, A multistep oriented attachment Kinetics: coarsening of ZnS nanoparticle in concentrated NaOH, J. Am. Chem. Soc. 128 (2006) 12981–12987.

[21] Z. Zhuang, J. Zhang, F. Huang, Y. Wang, Z. Lin, Pure multistep oriented attachment growth kinetics of surfactant-free SnO2 nanocrystals, Phys. Chem. Chem. Phys. 11 (2009) 8516–8521.

[22] Z. Liu, B. Lv, Y. Xu, D. Wu, Hexagonal a-Fe2O3 nanorods bound by high-index facets as high-performance electrochemical sensor, J. Mater. Chem. A 1 (2013) 3040–3046.

[23] H. Lv, R. Jiang, Y. Li, X. Zhang, J. Wang, Microemulsion-mediated hydrothermal growth of pagoda-like Fe3O4 microstructures and their application in a lithium–air battery, Ceram. Int. 41 (2015) 8843–8848.

[24] X.-L. Cheng, J.-S. Jiang, D.-M. Jiang, Z.-J. Zhao, Synthesis of rhombic dodecahedral Fe3O4 nanocrystals with exposed high-energy {110} facets and their peroxidase-like activity and lithium storage properties, J. Phys. Chem. C 118 (2014) 12588–12598.

[25] B. Maleki, S. Barat Nam Chalaki, S. Sedigh Ashrafi, E. Rezaee Seresht, F. Moeinpour, A. Khojastehnezhad, R. Tayebee, Caesium carbonate supported on hydroxyapatite-encapsulated Ni0.5Zn0.5Fe2O4 nanocrystallites as a novel magnetically basic catalyst for the one-pot synthesis of pyrazolo[1,2-b]phthalazine-5,10-diones, Appl. Organomet. Chem. 29 (2015) 290–295.

[26] W. Lv, W. He, X. Wang, Y. Niu, H. Cao, J.H. Dickerson, Z. Wang, Understanding the oriented-attachment growth of nanocrystals from an energy point of view: a review, Nanoscale 6 (2014) 2531–2547.

[27] H. Rietveld, Line profiles of neutron powder-diffraction peaks for structure refinement, Acta Crystallogr. 22 (1967) 151–152.

[28] L. Bleicher, J.M. Sasaki, C.O. Paiva Santos, Development of a graphical interface for the Rietveld refinement program DBWS, J. Appl. Crystallogr. 33 (2000) 1189.

[29] N.A.S. Nogueira, V.H.S. Utuni, Y.C. Silva, P.K. Kiyohara, I.F. Vasconcelos, M.A.R. Miranda, J.M. Sasaki, X-ray diffraction and Mossbauer studies on superparamagnetic nickel ferrite (NiFe2O4) obtained by the proteic sol–gel method, Mater. Chem. Phys. 163 (2015) 402–406.

[30] J. Wang, Prepare highly crystalline NiFe2O4 nanoparticles with improved magnetic properties, Mater. Sci. Eng. B 127 (2006) 81–84.

[31] K. Sangwal, Effect of impurities on the processes of crystal growth, J. Cryst. Growth 128 (1993) 1236–1244.

[32] O. Karaagac, B. Bilir, H. Kockar, Superparamagnetic cobalt ferrite nanoparticles: effect of temperature and base concentration, J. Supercond. Nov. Magnetism 28 (2015) 1021–1027.

[33] B.H. Toby, R factors in Rietveld analysis: how good is good enough? Powder Diffr. 21 (2006) 67–70.

[34] S.K. Pradhan, S. Bid, M. Gateshki, V. Petkov, Microstructure characterization and cation distribution of nanocrystalline magnesium ferrite prepared by ball milling, Mater. Chem. Phys. 93 (2005) 224–230.

[35] Y. Zhao, J. Zhang, Microstrain and grain-size analysis from diffraction peak width and graphical derivation of high-pressure thermomechanics, J. Appl. Crystallogr. 41 (2008) 1095–1108.

[36] A. Weibel, R. Bouchet, F. Boulc, P. Knauth, The big problem of small Particles: a comparison of methods for determination of particle size in nanocrystalline anatase powders, Chem. Mater. 17 (2005) 2378–2385.

[37] G.K. Williamson, W.H. Hall, X-ray line broadening from filed aluminium and wolfram, Acta Metall. 1 (1953) 22–31.

[38] Y. Zhao, Z. Qiu, J. Huang, Preparation and analysis of Fe3O4 magnetic nano-particles used as targeted-drug carriers, Chin. J. Chem. Eng. 16 (2008) 451–455.

[39] M.A. Amer, A. Tawfik, A.G. Mostafa, A.F. El-Shora, S.M. Zaki, Spectral studies of Co substituted Ni–Zn ferrites, J. Magn. Magn Mater. 323 (2011) 1445–1452.

[40] S.-G. Kim, W.-N. Wang, T. Iwaki, A. Yabuki, K. Okuyama, Low-temperature crystallization of barium ferrite nanoparticles by a sodium citrate-aided synthetic process, J. Phys. Chem. C 111 (2007) 10175–10180.

[41] H.-F. Yu, P.-C. Liu, Effects of pH and calcination temperatures on the formation of citrate-derived hexagonal barium ferrite particles, J. Alloys Compd. 416 (2006) 222–227.

[42] T. Nagase, K. Sakane, H. Wada, Effect of acids on crystallization of lithium borate films, J. Sol. Gel Sci. Technol. 8 (1997) 431–435.

[43] K. Maaz, A. Mumtaz, S.K. Hasanain, M.F. Bertino, Temperature dependent coercivity and magnetization of nickel ferrite nanoparticles, J. Magn. Magn Mater. 322 (2010) 2199–2202.

[44] S.K. Sharma, R. Kumar, S. Kumar, V.V. Siva Kumar, M. Knobel, V.R. Reddy, A. Banerjee, M. Singh, Magnetic study of Mg0.95Mn0.05Fe2O4 ferrite nano-particles, Solid State Commun. 141 (2007) 203–208.

[45] V. Kandasamy, V. Vellaiyappan Sangli Karuppanan, S. Sechassalom, Synthesis of nickel zinc iron nanoparticles by coprecipitation technique, Mater. Res. 13 (2010).

[46] R. Malik, S. Annapoorni, S. Lamba, V. Raghavendra Reddy, A. Gupta, P. Sharma, A. Inoue, Mössbauer and magnetic studies in nickel ferrite nanoparticles: ef-fect of size distribution, J. Magn. Magn Mater. 322 (2010) 3742–3747.

[47] M. Knobel, W.C. Nunes, L.M. Socolovsky, E. De Biasi, J.M. Vargas, J.C. Denardin, Superparamagnetism and other magnetic features in granular materials: a review on ideal and real systems, J. Nanosci. Nanotechnol. 8 (2008) 2836–2857.

[48] P.P. Naik, R.B. Tangsali, S.S. Meena, P. Bhatt, B. Sonaye, S. Sugur, Gamma ra-diation roused lattice contraction effects investigated by Mössbauer spec-troscopy in nanoparticle Mn–Zn ferrite, Radiat. Phys. Chem. 102 (2014) 147–152.

[49] C. Upadhyay, D. Mishra, H.C. Verma, S. Anand, R.P. Das, Effect of preparation conditions on formation of nanophase Ni–Zn ferrites through hydrothermal technique, J. Magn. Magn Mater. 260 (2003) 188–194.

[50] Z.Ž. Lazarević, Č. Jovalekić, V.N. Ivanovski, A. Rečnik, A. Milutinović, B. Cekić, N.Ž. Romčević, Characterization of partially inverse spinel ZnFe2O4 with high saturation magnetization synthesized via soft mechanochemically assisted route, J. Phys. Chem. Solid. 75 (2014) 869–877.

[51] V.G. Ivanov, M.V. Abrashev, M.N. Iliev, M.M. Gospodinov, J. Meen, M.I. Aroyo, Short-range B-site ordering in the inverse spinel ferrite NiFe₂O₄, Phys. Rev. B 82 (2010), 024104.

[52] Y. Yafet, C. Kittel, Antiferromagnetic arrangements in ferrites, Phys. Rev. 87 (1952) 290–294.

[53] Z.K. Heiba, M.B. Mohamed, M.A. Ahmed, M.A.A. Moussa, H.H. Hamdeh, Cation distribution and dielectric properties of nanocrystalline gallium substituted nickel ferrite, J. Alloys Compd. 586 (2014) 773–781.

[54] S. Kumar, A.M.M. Farea, K.M. Batoo, C.G. Lee, B.H. Koo, A. Yousef, Alimuddin, Mössbauer studies of Co0.5CdxFe2.5−xO4 (0.0⩽x⩽0.5) ferrite, Phys. B Con-dens. Matter 403 (2008) 3604–3607.

[55] Z. Lin, B. Gilbert, Q. Liu, G. Ren, F. Huang, A thermodynamically stable nanophase material, J. Am. Chem. Soc. 128 (2006) 6126–6131.

[56] R.L. Penn, J.F. Banfield, Imperfect oriented attachment: dislocation generation in defect-free nanocrystals, Science 281 (1998) 969–971.

[57] C.Z. Wagner, Z. Elektrochem, Theory of precipitate change by redissolution, Angew. Phys. Chem. 65 (1961) 581–591.

[58] M.V. Speight, Growth kinetics of grain-boundary precipitates, Acta Metall. 16 (1968) 133–135.

[59] H.O.K. Kirchner, Coarsening of grain-boundary precipitates, Metall. Trans. 2 (1971) 2861–2864.

[60] R. Aquino, F.A. Tourinho, R. Itri, M.C.F.L. e Lara, J. Depeyrot, Size control of MnFe2O4 nanoparticles in electric double layered magnetic fluid synthesis, J. Magn. Magn Mater. 252 (2002) 23–25.

[61] E.J.H. Lee, C. Ribeiro, E. Longo, E.R. Leite, Oriented Attachment: an effective mechanism in the formation of anisotropic nanocrystals, J. Phys. Chem. B 109 (2005) 20842–20846.

[62] L. Wu, P.-O. Jubert, D. Berman, W. Imaino, A. Nelson, H. Zhu, S. Zhang, S. Sun, Monolayer assembly of ferrimagnetic CoxFe3−xO4 nanocubes for magnetic recording, Nano Lett. 14 (2014) 3395–3399.

[63] K. Sue, M. Aoki, T. Sato, D. Nishio-Hamane, S.-i. Kawasaki, Y. Hakuta, Y. Takebayashi, S. Yoda, T. Furuya, T. Sato, T. Hiaki, Continuous hydrothermal synthesis of nickel ferrite nanoparticles using a central collision-type micro-mixer: effects of temperature, residence time, metal salt molality, and NaOH addition on conversion, particle size, and crystal phase, Ind. Eng. Chem. Res. 50 (2011) 9625–9631.

[64] N.T.K. Thanh, N. Maclean, S. Mahiddine, Mechanisms of nucleation and growth of nanoparticles in solution, Chem. Rev. 114 (2014) 7610–7630.

[65] Y. Wang, J. Zhang, Y. Yang, F. Huang, J. Zheng, D. Chen, F. Yan, Z. Lin, C. Wang, NaOH concentration effect on the oriented attachment growth kinetics of ZnS, J. Phys. Chem. B 111 (2007) 5290–5294.

[66] C. Ding, Y. Zeng, R. Li, Y. Zhang, L. Zhao, Temperature- and time-tuned morphological evolution of polyhedral magnetite nanocrystals and their facet-dependent high-rate performance for lithium-ion batteries, J. Alloys Compd. 676 (2016) 347–355.

[67] L. Wang, Y. Zhang, C. Cheng, X. Liu, H. Jiang, X. Wang, Highly sensitive elec-trochemical biosensor for evaluation of oxidative stress based on the nano-interface of graphene nanocomposites blended with gold, Fe3O4, and platinum nanoparticles, ACS Appl. Mater. Interface. 7 (2015) 18441–18449.

[68] A.J. Bard, L.R. Faulkner, Electrochemical Methods: Fundamentals and Appli-cations, Wiley, 2000.

[69] C. Srinivas, B.V. Tirupanyam, A. Satish, V. Seshubai, D.L. Sastry, O.F. Caltun, Effect of Ni2+ substitution on structural and magnetic properties of Ni–Zn ferrite nanoparticles, J. Magn. Magn Mater. 382 (2015) 15–19.

[70] A. Baykal, S. Güner, A. Demir, Synthesis and magneto-optical properties of triethylene glycol stabilized Mn1−xZnxFe2O4 nanoparticles, J. Alloys Compd. 619 (2015) 5–11.

[71] S. Güner, S. Esir, A. Baykal, A. Demir, Y. Bakis, Magneto-optical properties of Cu1−xZnxFe2O4 nanoparticles, Superlattice. Microst. 74 (2014) 184–197.

[72] C. Pereira, A.M. Pereira, C. Fernandes, M. Rocha, R. Mendes, M.P. Fernández-García, A. Guedes, P.B. Tavares, J.-M. Grenèche, J.P. Araújo, C. Freire, Super-paramagnetic MFe2O4 (M = Fe, Co, Mn) nanoparticles: tuning the particle size and magnetic properties through a novel one-step coprecipitation route, Chem. Mater. 24 (2012) 1496–1504.

[73] N. Jovic, B. Antic, G.F. Goya, V. Spasojevic, Magnetic properties of lithium ferrite nanoparticles with a core/shell structure, Curr. Nanosci. 8 (2012) 651–658.

[74] V. Sreeja, S. Vijayanand, S. Deka, P.A. Joy, Magnetic and Mössbauer spectro-scopic studies of NiZn ferrite nanoparticles synthesized by a combustion method, in: N.S. Gajbhiye, S.K. Date (Eds.), ICAME 2007, Springer Berlin Hei-delberg, 2009, pp. 271–279.

[75] R.D. Sánchez, J. Rivas, P. Vaqueiro, M.A. López-Quintela, D. Caeiro, Particle size effects on magnetic properties of yttrium iron garnets prepared by a sol–gel method, J. Magn. Magn Mater. 247 (2002) 92–98.

[76] C. Caizer, M. Stefanescu, Magnetic characterization of nanocrystalline Ni–Zn ferrite powder prepared by the glyoxylate precursor method, J. Phys. D Appl. Phys. 35 (2002) 3035.